Predicting the Diameters of Droplets Produced in Turbulent Liquid-Liquid Dispersion

John A. Thomas[1*], Brian DeVincentis[1], Johannes Wutz[2], Francesco Ricci[3]

1) M-Star Simulations, LLC 10020 Baltimore National Pike, Ellicott City, MD 21042-, USA
2) M-Star Center Europe, GmbH Hauptstrasse 3, 38822 Sargstedt, Germany
3) Boehringer Ingelheim Pharmaceuticals, Inc 900 Ridgebury Road, Ridgefield, CT 06877
*Corresponding author: thomas@mstarcfd.com

Abstract

The droplet size distribution in liquid-liquid dispersions is a complex convolution of impeller speed, impeller type, fluid properties, and flow conditions. In this work, we present three a priori modeling approaches for predicting the droplet diameter distributions as a function of system operating conditions. In the first approach, called the two-fluid approach, we use high-resolution solutions to the Navier-Stokes equations to directly model the flow of each phase and the corresponding droplet breakup/coalescence events. In the second approach, based on an Eulerian-Lagrangian model, we describe the dispersed fluid as individual spheres undergoing ongoing breakup and coalescence events per user-defined interaction kernels. In the third approach, called the Eulerian-Parcel model, we model a sub-set of the droplets in the Eulerian-Lagrangian model to estimate the overall behavior of the entire droplet population. We discuss output from each model within the context of predictions from first principles turbulence theory and measured data.

1.0 Introduction

Liquid-liquid separations and extractions are often performed as batch processes inside agitated tanks. (1) Within such systems, droplet formation depends on the physical properties of the two fluids, as well as the fluid mechanical environment established by the impeller. (2) (3) In non-coalescing systems, the droplet size distribution and corresponding mean droplet diameter shift to smaller values as droplets repeatedly pass though regions of high energy dissipation near the impeller. (4) Eventually, after all droplets pass through the trailing vortex, a steady-state mean droplet size and system-level droplet size distribution is produced. (5) In coalescing systems, the ongoing competition between droplet breakup and droplet coalescence produces a steady-state size distribution that varies as a function of position within the tank. Successful process design requires accurately predicting these droplet size distributions as a function of fluid properties, system topology, and operation conditions.

The importance of these processes has motivated the development of numerical models for predicting droplet sizes within agitated tanks. Most of these modeling efforts have focused on a hybridization of Reynolds Average Navier-Stokes (RANS) fluid models for describing the

continuous phase with population balance models (PBM) for describing droplet break-up and coalescence. (6) Although this time-averaged approach reduces the computational complexity of the problem, it presents multiple abstractions and assumptions that are worth inspecting. (7) Most importantly, this approach assumes that droplets move through a static, time-averaged flow field with a time-independent energy dissipation landscape. In reality, the flow field and energy dissipation profiles across a turbulent tank are constantly evolving. (8) For example, depending on the instantaneous angular position of the impeller, two droplets at the same physical location in the tank but at different times can experience order-of-magnitude variations in local energy dissipation rate. Since the droplet size is a non-linear function of energy dissipation, the time-averaged input will distort spatiotemporal variations in droplet size. (9) Moreover, droplets are discrete objects that interact directly with the fluid and other droplets to undergo discrete break-up and coalescence events. Recasting this discrete population set into a continuous probability density function makes systems with low and/or strongly varying particle number densities difficult to handle using RANS-PBM approaches. Lastly, among the large number of proposed PBM closure formalisms, (10) the user-defined parameters that should be specified to model a specific system are not obvious. (11)

In this paper we present a set of unified, time-accurate, physics-based modeling approaches for predicting the dispersion properties of immiscible fluids in dynamic systems. Of particular interest are turbulent, two-fluid systems in agitated tanks with volumes ranging from 0.1 L to 1000 L and dispersed-phase droplet diameters between 10-1000 micrometers. Using these models, we seek to predict the dispersed phase droplet size distribution as a function of fluid properties, operating conditions, and system scale with no reparameterization or model tuning between scales or operating conditions. We also seek to eliminate user-defined parameters, using only physical properties and expectations from first principles turbulence theory as model input. We focus our work on algorithms which are amenable to graphics processing unit-based computing. (8) (12)

We begin in Section 2 with a review of the relevant physics driving dispersion processes. This background will act as validation for the models that follow, with respect to the mean droplet size and droplet size distribution. In Section 3, we present results from a high-resolution, Eulerian-Eulerian simulation of a two immiscible fluid blending simulation in a lab-scale agitated tank. This direct two-fluid approach solves the time-accurate Navier-Stokes equations using fluid properties and system operating conditions as the only model inputs. The droplet sizes predicted from this model, as well as the droplet breakup kinetics, are shown to agree with measured data and expectations from turbulence theory. Although the computational memory requirements limit the practical application of this approach to fluid volumes below 1-10 L, the breakup kinetics can be used to inform more scalable modeling approaches.

In Section 4, we present an Eulerian-Lagrangian (E-L) approach for describing fluid mixing and droplet formation. In this approach, the dispersed phase is described using individually tracked particles that evolve according to Newton's second law. Like the direct two-fluid approach, the E-L approach can handle fluids with differing density and rheology by calculating a continuous dispersed phase volume fraction. Using breakup kernels corroborated by the direct two-fluid approach, the E-L model can also handle droplet breakup/coalescence and predict the corresponding droplet size distribution. Since the fluid interface between the two fluids is not resolved explicitly in the E-L approach, the computational demands of the E-L approach are orders-of-magnitude smaller than those of the direct two-fluid approach. However, since all droplet dynamics and collisions are resolved explicitly, memory constraints limit the applicability of this approach to fluid volumes below 10-100 L.

In Section 5, we present an Eulerian-Parcel (E-P) extension of the E-L model. A droplet parcel is a single Lagrangian point object that represents the motion of a larger group of individual droplets. Like the E-L approach, the dispersed phase in the E-P model is described by a set of individually tracked parcels that evolve according to Newton's second law. The approach can similarly be used to handle fluids with differing density and rheology by reconstructing a continuous dispersed phase volume fraction. In contrast to these models, however, not every

droplet in the E-P approach is modeled explicitly. Rather, changes in the parcel diameter inform the parcel number scale---a value that describes the number of real droplets represented by the parcel. This coarse-grained approach to droplet tracking reduces the computational requirements of the E-P model by multiple orders-of-magnitude relative to the E-L model. The abstractions introduced by the parcel model, however, introduce complexities when modeling coalescence. We conclude in Section 6 with comments on generality.

2.0 Dispersion Overview

In turbulent systems, droplets are formed by dynamic pressure forces stemming from spatial variations in the continuous phase fluid velocity. The size of the resulting droplets, D_m, is related to the length-scale of these velocity variations. More specifically, D_m represents the size of the largest droplet for which the stabilizing effects of surface tension exceed the stretching effects of the flow. This competition between surface tension and fluid motion can be described using the Weber number: (13)

$$We = \frac{\rho u^2 D_m}{\sigma} \qquad \text{Eqn. (1)}$$

where ρ is the density of the continuous phase, σ is the surface tension between the two fluids, and u^2 represents the square of the velocity difference in the continuous phase over the length D_p. Per Equation 1, breakup is assumed to occur above some critical Weber number. Below this critical value, droplets will be stable against the spatial variation in the flow field.

If the droplet is small, such that the surrounding turbulent velocity field is isotropic and homogeneous, the velocity of the continuous phase fluid surrounding the droplet can be related to the specific energy dissipation rate, ε, such that: (14)

$$v \approx (\varepsilon D_m)^{\frac{1}{3}} \qquad \text{Eqn. (2)}$$

Combining Equations 1 and 2 gives:

$$D_m = C_1 \frac{\sigma^{\frac{3}{5}}}{\rho^{\frac{3}{5}} \varepsilon^{\frac{2}{5}}} \qquad \text{Eqn. (3)}$$

where C_1 is a constant value related to the critical Weber number. This expression indicates that, for a constant surface tension and density, the maximum stable droplet diameter tends to

decrease with increasing local energy dissipation rate. Similarly, for a constant energy dissipation rate, increasing the surface tension tends to increase the maximum stable droplet diameter. The coefficient C_1 is determined experimentally as 0.725. (15) This semi-empirical relationship is used frequently in droplet and bubble size distribution correlations. (13)

Measured droplet size data from turbulent liquid-liquid dispersion processes corroborates these expectations from first principles turbulence theory. Work by Sprow, who measured the droplet diameter distribution produced near a flat blade impeller of a non-coalescing isooctane/saltwater emulsion, suggested the following empirical relationship: (5)

$$d_{32} = C_2 \frac{\sigma^{\frac{3}{5}}}{\rho^{\frac{3}{5}} N^{\frac{6}{5}} D^{\frac{4}{5}}} \qquad \text{Eqn. (4)}$$

where d_{32} is the Sauter mean diameter of the droplets, ρ is the continuous phase fluid density, N is the impeller speed, and D is the impeller diameter. The dimensionless cofactor C_2 is a function of the system topology and the measurement location relative to the impeller. For non-coalescing systems C_2 is approximately 0.05. For actively coalescing systems, C_2 = 0.05-0.15 depending on measurement location. (4)

Although Equation 4 is written in terms of operating parameters and is specific to flat blade impellers, the functional form follows the theoretical model presented in Equation 3. Recognize that, in an agitated tank, the average specific energy dissipation rate around the impeller can be estimated from:

$$\varepsilon \approx N^3 D^2. \qquad \text{Eqn. (5)}$$

Substituting Equation 5 into Equation 4 recovers the empirical relationship presented in Equation 3:

$$D_m = C_1 \frac{\sigma^{\frac{3}{5}}}{\rho^{\frac{3}{5}} \varepsilon^{\frac{2}{5}}} = C_3 \frac{\sigma^{\frac{3}{5}}}{\rho^{\frac{3}{5}} (N^3 D^2)^{\frac{2}{5}}} = C_3 \frac{\sigma^{\frac{3}{5}}}{\rho^{\frac{3}{5}} N^{\frac{6}{5}} D^{\frac{4}{5}}} \qquad \text{Eqn. (6)}$$

where C_3 is a proportionality constant specific to the system topology. Other reports have identified a similar relationship between first-principles turbulence theory and mean droplet diameter. (16)

In non-coalescing systems, droplet diameters will converge to the minimum diameter prescribed by the maximum energy dissipation rate realized in the tank. The time required to complete this breakup process will therefore be a function of the recirculation time through these high energy dissipation rate regions. In coalescing systems, the steady-state droplet diameter distribution will represent the competition between bubble breakup due to energy dissipation rates and bubble coalescence. Both these points will be discussed below.

3.0 Direct Two-Fluid Model

3.1 Mathematical Description

To understand and validate the relationships presented in Section 2, we seek to model the transient, three-dimensional dispersion process of an immiscible, viscous, two-fluid system through direct application of the Naiver-Stokes equations. At this level, the mechanics of the two-fluid system are governed by the conservation of mass and momentum equations:

$$\nabla \cdot \vec{u} = 0 \qquad \text{Eqn. (7)}$$

$$\frac{\partial \vec{u}}{\partial t} + \vec{u} \cdot \nabla \vec{u} = -\frac{1}{\rho}\nabla p + \frac{1}{\rho}\nabla \cdot [\mu(\nabla \vec{u} + \nabla^T \vec{u})] + \frac{1}{\rho}\vec{F}_b + \frac{1}{\rho}\vec{F}_s \qquad \text{Eqn. (8)}$$

where ρ is the density, $\vec{u}$ is the velocity, p is the pressure, μ is the dynamic viscosity, $\vec{F}_b$ is the body force, $\vec{F}_s$ is the surface force, and t is time. The density and viscosity at each point in the system are defined from:

$$\rho = \rho_1 + \phi(\rho_2 - \rho_1) \qquad \text{Eqn. (9)}$$

$$\mu = \mu_1 + \phi(\mu_2 - \mu_1) \qquad \text{Eqn. (10)}$$

where subscripts 1 and 2 refer to the continuous and dispersed phases, respectively, and ϕ is a spatially varying marker function defining the volume fraction of the dispersed fluid. The time-evolution of ϕ is governed by a conservative phase field equation (17).

Equations 7 and 8 are solved using the cumulative lattice Boltzmann method. (18) This lattice-based implementation introduces δ_x and δ_t as two user-defined simulation parameters. The lattice spacing δ_x defines the spatial resolution of the simulation. Within the direct two-fluid approach considered here, this value characterizes the minimum droplet diameter that can be resolved explicitly within the flow domain. To maximize the spectrum of droplets that can be

captured by the simulation, δ_x in the direct two-fluid model should be as small as computationally practical. The lattice timestep δ_t, which defines the compressibility of the fluid, is informed by the CFL condition: (19)

$$C_m = \frac{V_r \delta_t}{\delta_x} < 1 \qquad \text{Eqn. (11)}$$

where V_r is a reference velocity (taken here to be the impeller tip speed) and C_m is the Courant number. In this work, the Courant number was set to 0.05, a value sufficient to keep the maximum density fluctuations below 1%.

Fluids interact with the tank walls via a no-slip boundary condition, as enforced via a zero-velocity bounce back method. (20) Fluids interact with the moving impeller via the immersed boundary method, which enforces a no-slip velocity boundary condition along the impeller/shaft surfaces as they move through the fluid. (21) The free slip boundary condition is applied to the top of the fluid domain. Since the systems here are well baffled, a free-surface model is not necessary. Turbulence is modeled use large eddy simulation (LES) with a Smagorinsky coefficient C_s of 0.1. (14) (22) The computational models were built and solved using M-Star CFD®, a GPU-based computational physics package tailored for chemical engineering simulations. (23)

3.2 Model Set-up

In Figure 1, we present the geometry of the 1 L system used to perform the direct two-fluid simulations. The vessel diameter and height were both 0.1-m with four equally spaced 0.01-m baffles attached to the tank wall. The impeller was positioned at the center of the vessel and elevated 0.033 m off the tank bottom. We modeled a standard Rushton impeller with a diameter of 0.033 m and blade width/height shown in the figure. The impeller speed was set to 400 RPM. The lattice spacing was set to 150 μm, which corresponded to about 297 million grid points across the simulation domain. This resolution is sufficient to resolve droplets down to 150 μm, a point discussed in more detail below. We note that this lattice size exceeds the resolution required to predict grid-independent impeller power number and bulk flow characteristics. (24) (25)

Both fluids were assigned a density and viscosity of 1000 kg/m^3 and 10^{-6} m^2/s. The surface tension between the fluids was set to 0.04 N/m. (26) The initial volume fraction of dispersed phase was set to 1.0 within the 0.01 m-diameter sphere, as indicated in Figure 1. Since the system is closed, the total volume of each fluid remains constant for the duration of the simulation. The effects of agitation, however, will cause the dispersed fluid to breakup into droplets. Recognize that the impeller Reynolds number is 7300, suggesting that the flow field inside the vessel will be turbulent.

3.2 Model Output

In Figure 2, we present a snapshot of the velocity, energy dissipation rate, and dispersed phase volume fraction after 10 seconds of agitation. As expected, the fluid respects the no-slip boundary condition: adjacent to the tip of the impeller, the fluid velocity is linked to the impeller tip speed (0.69 m/s in this case). At the tank wall, the velocity is zero. These results are expected, given that we are modeling a fully transient system. Between these two extremes the velocity varies as a function of position relative to the impeller.

The dimensionless impeller power number, P_o, for this system is calculated from:

$$P_o = \frac{\tau\omega}{\rho N^3 D^5} \qquad \text{Eqn. (12)}$$

where τ is the torque on the impeller, ω is the angular velocity, N is the impeller speed and D is the impeller diameter. The predicted power input for the system, which represents the numerator of Equation 12, is calculated to be 0.052 W. The corresponding power number is therefore predicted to be 4.5, a value inline with power numbers for similar systems. (27)

During steady state operating conditions, this input power is equal to the power dissipation across the tank. In each lattice voxel i, the specific energy dissipation rate ε_i is calculated from:

$$\varepsilon_i = \nu_i \bar{S}_i^2 \qquad \text{Eqn. (13)}$$

where ν_i is the local kinematic viscosity. Note that this local kinematic viscosity includes contributions from both the molecular and eddy viscosities. The total power dissipation across the tank is calculated from the volume integral of the local energy dissipation rate:

$$E_t = \iiint \rho \varepsilon_i dV \quad \text{Eqn. (14)}$$

where ε_i represents the specific energy dissipation rate at the individual lattice voxel i and dV represents the voxel volume. The total energy dissipation calculated using Equation 14 is 0.05 W, a value within 4% of the input shaft power used in Equation 12. This agreement confirms that, to sufficient accuracy, the solver conserves total system energy.

Note that, in the trailing vortex, the energy dissipation rate is on the order of 1-3 W/kg. To validate this prediction, we compare this output to experimentally measured dissipation rates for similar impellers. From the measurements of Grenville, the average energy dissipation rate in the trailing vortex, ε_m, can be calculated from: (16)

$$\varepsilon_m = \frac{P_o N^3 D^3}{4 w_p}, \quad \text{Eqn. (15)}$$

where w_p is the width of the impeller blade. Recognize that Equation 15 presents the scaling cofactor for the proportionality relationship originally presented in Equation 5. Using the predicted power number of 4.5 and the blade width of 8.25 mm, ε_m calculated from this correlation is 1.4 W/kg. This value is in-line with the range of values presented in Figure 2. Above this mean value, however, certain locations within the trailing vortex are predicted to realize instantaneous energy dissipation rates approaching 10 W/kg.

This alignment between (i) the predicted/measured power numbers, (ii) the predicted total power input/dissipation, (iii) the predicted/measured specific energy dissipation rates in the trailing vortex suggest that energy transfer and dissipation are handled properly in the simulation. This agreement is important, as variations in energy dissipation rates are correlated to large variations in droplet size. Within the trailing vortex, droplet diameters are on the order of 200-300 µm. Further from the impeller, where the energy dissipation rate is order-of-magnitude smaller, droplet diameters are order-of-magnitude larger. This pattern suggests

that, for coalescing systems, the droplet size distribution is a function of position within the tank. This variation has been observed experimentally. (4)

3.3 Droplet Formation and Dynamics

In Figure 3, we plot the Sauter mean droplet diameter versus the average energy dissipation rate along the surface of each droplet. This data represents the aggregation of 23,000 droplets individually identified over 5 seconds of steady-state agitation. The shape of this distribution function represents the ongoing competition between breakup, coalescence, energy dissipation, and impeller pumping. Mechanistically speaking, the evolution of an individual droplet through the tank can be explained by tracing it clockwise through the four quadrants of this scatter plot.

To begin, consider the top-left quadrant of the distribution, which represents large droplets in regions with low energy dissipation rates (near the top and bottom of the tank). The pumping action of the impeller draws these large droplets towards the impeller into regions with elevated energy dissipation rates. As droplets move near the impeller, the maximum droplet diameter stable against the local energy dissipation rate decreases. This imbalance leads to breakup into increasingly small daughter particles, driving the droplets towards the bottom-right quadrant of the distribution.

To contextualize this trajectory, we superimpose Equation 3 onto Figure 3 using the surface tension and density specified in the simulation (0.04 N/m and 1000 kg/m^3). The variation in maximum droplet diameter with energy dissipation, as expected from this first-principles model, is consistent with predictions from the direct two-fluid simulation. Within the context of this two-fluid model, this relationship between droplet size and energy dissipation is neither enforced nor proscribed when modeling fluid motion. The consistency with turbulence theory, however, suggests that the simulation is properly capturing the droplet breakup in response to changes in the local energy dissipation rate.

The pumping action of the impeller eventually pulls droplets into the trailing vortex, which has an energy dissipation rate characterized by Equation 15. Although ephemeral points with higher energy dissipation rates exist in the system, Equation 15 is representative of the maximum energy dissipation rate realized in the system. As such, as illustrated in Figure 3, Equation 15 characterizes the average energy dissipation rate (and corresponding droplet diameter) sampled by the dispersed phase within the trailing vortex. Recognize that Equation 15 is neither enforced nor proscribed when solving the fluid motion and predicting the two-fluid dynamics. The agreement, however, between the design correlation and the energy dissipation rate sampled by the fluid in the trailing vortex, however, corroborates the simulation predictions.

Small droplets exiting the trailing vortex are discharged back up the tank sidewalls to regions with lower energy dissipation rates. Within the context of Figure 2, this motion represents a transition from the high-EDR bottom-right quadrant to the low-EDR bottom-left quadrant. Note that these small droplets are not produced in the bottom-left quadrant, as the energy dissipation rates in these regions are insufficient to form droplets this small. Rather, the pumping action of the impeller pushes these small droplets away from the trailing vortex into regions with lower energy dissipation rates. These regions of lower energy dissipation permit coalescence and the development of larger droplets. Within the simulation, ongoing coalescence in the low EDR regions cause droplets to grow until they return to the top-left quadrant. The process then repeats as these droplets are drawn back into the trailing vortex.

The minimum droplet size that can be resolved by the solver is related to the simulation lattice spacing δ_x. To understand the effects of this limitation, in Figure 4 we present a histogram of the droplet diameter. This plot is generated by integrating the scatter plot presented in Figure 3 over all energy dissipation rates (*i.e.* the x-axis). The droplet size distribution is non-uniform, with a most probable droplet diameter of 300 μm and a mean droplet diameter of 600 μm. At these operating conditions, most of the droplets are above the numerical floor presented by the grid resolution. If the impeller were operated at a much higher speed---which would be

expected to produce smaller droplets---this grid resolution would be insufficient to properly resolve the droplet size distribution. This coupling between resolution, droplet size, and impeller speed limits the scalability of the direct two-fluid approach, a point we discuss below.

To contextualize this data, we superimpose on this histogram the droplet diameter predicted by combining Equations 3 with the maximum energy dissipation rate realized in the trailing vortex (~10 W/kg). We also superimpose the experimental design correlation presented in Equation 4. We apply a cofactor of 0.1 to this expression, which is in-line with the measured values across the tank for coalescing systems. (4) Recognize that the correlation presented in Equation 4 was developed using a flat-blade impeller as opposed to the Rushton considered in the numerical model used here. This difference will bias predictions from the correlation to lower droplet sizes. The overall consistency between the mean droplet size predicted from the direct two-fluid model, turbulence theory, and literature correlation suggest that the algorithm is correctly capturing the competition between energy dissipation and droplet surface tension.

3.4 Examining Breakup

In addition to predicting the steady-state droplet size distribution, the direct two-fluid model can be used to track individual droplets moving through the vessel as they undergo discrete breakup events. From this data, it is possible to understand the relative volume fractions of the daughter droplets generated during breakup. In Figure 5, we present a time-integrated plot of a single large droplet entering the trailing vortex and breaking up to form many smaller droplets. Each line represents an individual daughter droplet with a line thickness corresponding to the droplet diameter. This plot corresponds to 2 second of fluid motion, a duration sufficient for fluid to enter and fully exit the trailing vortex.

The trajectory of these particles is aligned with the data presented in Figure 3: as the large droplet enters the trailing vortex, it breaks-up into many smaller droplets. These smaller droplets then exit the trailing vortex and coalesce to form larger droplets in regions of the vessel with lower energy dissipation rates. We find that approximately 95% of all breakup

events occurred as binary daughter formations, wherein an individual breakup event created one (new) additional droplet. This behavior is consistent with experimental observation for the low Weber number droplets considered here. (28)

We also present in Figure 5 the daughter droplet volume fractions, f_v, realized by tracking 20,000 individual binary droplet breakup events. As expected from the conservation of volume, the distribution is symmetric: any volume not in the first daughter droplet must be occupied by the second daughter droplet. The M-shape of this distribution function indicates that most breakup events follow an approximately 95%/5% volume split of the initial droplet volume. Mechanistically speaking, as a droplet enters regions wherein the local turbulent energy dissipation rate exceeds the stabilizing effects of surface tension, the droplet breakup process resembles small satellite formation rather than large-scale droplet splitting.

We superimpose on this data the daughter volume fraction predictions from first principles turbulence theory. This theoretical model, as presented by Xing et al., uses the Young–Laplace and Bernoulli equations to model internal flow through the droplet neck during a breakup event. (29) Within this approach, the probability of a droplet of diameter d breaking into a daughter droplet with breakup fraction f_v becomes a function of the surface tension, fluid densities, fluid viscosity, and local energy dissipation rate. To calculate the distribution using the Unified Breakup Model presented in Figure 5, we used the energy dissipation rate computed from Equation 15 and the mean droplet diameter computed from Figure 4.

The key finding from the Unified Breakup Model, which is consistent with distributions in the original report by Xing, is that the probability distribution is M-Shaped with a minimum at 0.5 and a maximum around 0.9. That is, at the operating conditions considered here, droplet breakup events tend to be highly asymmetric with one daughter droplet hosting most of the initial droplet volume. We recognize that the breakup volume fraction distribution calculated from the direct two-fluid model presents a larger variance than predictions from the Unified Breakup Model. We also note that the locations of the peaks in the daughter volume fraction

probability density function differ by approximately 10%. The overall shapes of the distributions, however, are consistent and contrast the uniform and/or triangle-shaped breakup volume fractions realized at higher energy dissipation rates and/or lower surface tensions. Motivated by this consistency, the Unified Breakup Model will become an important part of the particle-based approaches considered later in Sections 4 and 5.

3.5 Advantages and Disadvantages

The direct two-fluid model presented in this section reproduces many of the key physics measured during experiment and predicted from first principles turbulence theory. The only model input parameters are fluid properties, system geometry, and operating conditions. In this way, the approach is ideal for developing/understanding two-fluid blending, droplet formation, and droplet transport processes. These model outputs can then be used to understand the physics driving dispersion of systems with little experimental reference data. Moreover, because the volume fraction is continuous and considered at each lattice site, the approach can handle arbitrary fluid volume fractions.

Although robust, the approach is limited by resolution and the range of length scales relevant to the system. At the smaller end of this range, the simulation must resolve the smallest droplets in the system. At the upper end of this range, the simulation must extend the entire tank domain. As discussed above, this 1 L system considered here required 297 million lattice points to resolve droplet diameters down to 0.15 mm. On a compute node with 8 NVIDIA V100 GPUs, the two-fluid simulations advanced at approximately 1 billion lattice updates per second. For this lab-scale model, this speed corresponded to 10 impeller turns per day of simulation time. In principle, the total simulation capacity for this compute node is approximately 500 million lattice points---2x larger than the system considered here. In practice, however, production-sized equipment may have orders-of-magnitude larger operating volumes. Moreover, depending on the impeller tip speed and/or shape, the associated droplets sizes may be smaller relative to those realized in this system. These effects increase the required resolution and can make a simulation computationally intractable. Thus, although the direct

two-fluid model is useful for researching the first-principles physics governing droplet dynamics at laboratory scale, a more scalable approach is required to model larger systems.

4.0 Eulerian-Lagrangian Simulations

4.1 Conceptual Overview

To overcome the resolution requirements of the direct two-fluid model, we now develop and propose a E-L approach for modeling two-fluid mixing and droplet dispersion processes. Within this approach, the continuous phase is still modeled as an Eulerian fluid. The dispersed phase, however, is modeled using a *large number* of *initially monodisperse*, *individually tracked* particles which undergo breakup and pairwise coalescence events. By *large number*, we imply that the particle number density is sufficient to reconstruct a continuous dispersed fluid volume fraction across the tank. By *initially monodisperse*, we imply that the initial droplet diameters are all identical but evolve over time to form a steady-state droplet size distribution. By *individually tracked* we mean that the position and velocity of all particles are tracked in real-time with breakup and coalescence relationships defined *a priori*.

4.2 Mathematical Description

As with the direct two-fluid model, the fluid mechanics of the continuous phase in the E-L model are described by the incompressible Navier-Stokes equations. Unlike Equation 8, however, fluid model here does not include the surface tension force since the two-fluid interface is not resolved explicitly. The Lagrangian dispersed phase particles are described using a cherry-pit model. (30) Within this approach, each dispersed phase particle has a rigid core that interacts elastically with the rigid cores of other dispersed-phase particles. The purpose of the hard sphere interactions is to ensure that the initial dispersed phase volume remains incompressible prior to droplet breakup/dispersion. Surrounding each rigid core is a fully penetrable concentric exterior shell that increases the apparent volume of the particle. The purpose of the shell is to allow the dispersed phase volume fraction to overcome the 0.62 limit on volume fraction presented by random sphere packing. (31) That is, by accounting for the

interstitial region between a random pack of rigid spheres, the dispersed phase volume fraction reconstructed from the cherry-pit particles can realize values close to 1.0.

As illustrated in Figure 6, the dispersed phased particles enter the system as a random close pack of monodisperse particles within a pre-defined initial volume. The initial total droplet diameter within this volume, $D_{T,o}$ represents the maximum diameter of the dispersed phase droplets resolved by the simulation. We set this initial value to the simulation lattice spacing, which is sufficient to reconstruct a continuous dispersed phase fluid volume fraction. With this initial diameter defined, the total number of dispersed phase particles initially added to the system is calculated from:

$$N_{t,o} = \frac{\phi_f V_o}{\frac{\pi}{6} D_{T,o}^3} \quad \text{Eqn. (16)}$$

where ϕ_f is the user-set initial volume fraction of the dispersed phase in the pre-defined initial volume V_o. We set ϕ_f to 1.0, which implies that the initial injection fluid volume contains 100% dispersed phase fluid.

For a given particle diameter, the corresponding rigid core diameter, d_c is defined from:

$$d_c = \phi_p^{\frac{1}{3}} D_{T,o} \quad \text{Eqn. (17)}$$

where ϕ_p is the hard sphere packing fraction taken here to be 0.62. The reconstructed dispersed phase volume fraction at each fluid voxel j is calculated from:

$$\phi_j = \frac{\sum_i^{i \in j} V_{P,i}}{V_j} \quad \text{Eqn. (18)}$$

where $V_{P,i}$ is the volume of droplet i calculated using D_P, V_j is the volume of voxel j, and $i \in j$ is the list of dispersed phase particles with centers of mass contained in voxel j. The dispersed phase volume fraction defined in Equation 18 is calculated at each simulation time step.

The trajectory of each particle is governed by Newton's second law, such that:

$$m_i \vec{a}_i = \vec{F}_{i,g} + \vec{F}_{i,a} + \vec{F}_{i,p} + \vec{F}_{i,D} + \vec{F}_{ij} \quad \text{Eqn. (19)}$$

where m_i and $\vec{a}_i$ represent the mass and acceleration vector of droplet i, $\vec{F}_{i,g}$ is the gravity force, $\vec{F}_{i,a}$ is the added mass force, $\vec{F}_{i,p}$, is the instantaneous pressure gradient force, and $\vec{F}_{i,D}$ is the instantaneous drag force on the droplet, and $\vec{F}_{ij}$ is the collision force between hard rigid cores. The gravity, added mass, pressure gradient, and drag forces are the same as those reported in the literature. (32) The collision force is modeled as using a hard-sphere potential with a stiffness that limits overlap to less than 1% the droplet diameter. (33) Equation 19 is solved for each droplet individually and in tandem with the fluid algorithm using the velocity Verlet algorithm. (33)

Droplets perform a neighbor search using a bounding volume hierarchy (BVH) data structure. (12) The BVH is a binary tree in which each node stores a bounding box encompassing all nodes beneath it. Each droplet traverses the BVH using a binary search algorithm. This approach is efficient, has low memory requirements, and easily handles any spatial distribution of droplets. Additionally, the algorithms used to construct and traverse the BVH are easily implemented in a parallel fashion on GPUs. Using this approach, we find that simulations containing hundreds of millions of interacting droplets are practical on multi-GPU desktop computers.

In accordance with Newton's third law, droplets are two-way coupled to the fluid, such that a body force at each fluid lattice voxel j, $\vec{F}_{f,j}$:

$$\vec{F}_{f,j} = -\sum_i^{i \in j} \left(\vec{F}_{i,a} + \vec{F}_{i,D}\right) \qquad \text{Eqn. (20)}$$

is superimposed on the fluid lattice voxel j containing the set of droplets $i \in j$.

4.3 Model Set-up

The impeller and tank topology are the same as the 1 L system presented in Figure 1. We apply a lattice spacing of 0.667 mm, which is sufficient to properly resolve flow and energy dissipation across the vessel. (24) (25) Since we are only solving for the time-evolution of the continuous phase, this 4x coarsening of the lattice spacing generates a computational domain that is 64x smaller than the domain used to model the direct two-fluid simulations. Moreover, the timestep in these E-L simulations is 4x larger than those applied in the direct two-fluid

simulations. The combined effect of these changes is a 256x reduction in runtime the Navier-Stokes equations.

The initial dispersed phase volume was created by packing the initial volume with 2,000,000 individual droplets with an initial diameter $D_{T,o}$ of 0.334 mm. The particle core diameter and shell thickness were 0.285 mm and 0.0254 mm, which corresponds to a hard sphere packing fraction of 0.62 and a dispersed phase volume fraction of 1.0. The particle tracking, breakup, and coalescence algorithms active in the E-L model introduce computational requirements that are not present in the direct two-fluid model. Thus, although time is saved on the continuous phase, new computational bottlenecks are introduced via the particle algorithm. This point is discussed in more detail below.

4.2 Reconstructing the Volume Fraction

We begin by demonstrating how the dispersed phase volume fraction is reconstructed from the discrete phase droplet particles. This reconstruction is a pre-requisite for calculating any spatial variations in density and viscosity and their corresponding effects on fluid flow. Breakup and coalescence are disabled in this simulation, meaning the diameter of the droplets was constant throughout the mixing process. As with the direct two-fluid model, both fluids were assigned a density and viscosity of 1000 kg/m^3 and 10^{-6} m^2/s. For the purposes of testing the dispersed phase reconstruction, the volume of the dispersed fluid was increased to 40 mL (0.05 volume fraction) and initially centered at the top of the vessel.

At the start of the simulation, as illustrated in Figure 7, the Lagrangian particles representing the dispersed phase are aggregated within the initial fluid volume. As expected, the corresponding dispersed fluid volume fraction throughout this region is within a few percent of 1.0. Because the system is closed, the total volume of the dispersed phase remains equal to the initial 40 mL throughout the blending process. With time, however, the pumping action of the impeller stretches the dispersed fluid towards the trailing vortex and causes the droplets to disperse. After approximately 15 seconds of agitation, particles are uniformly distributed across

the vessel. This predicted homogenization timescale is inline with the 14.8 second blend time expected from experimental design correlations. (34)

To further contextualize these results, we present the time-evolution of a weightless dye moving through this same system according to the advection-diffusion equation. The advection-diffusion equation, which models the conservation of species, can be written as:

$$\frac{\partial c}{\partial t} + \nabla \cdot \left(\vec{V} c\right) = \nabla \cdot (D \nabla c) \qquad \text{Eqn. (21)}$$

Where c represents the local species concentration and D is the local diffusion coefficient. This equation is inherently transient: the left-hand side represents the time rate of species change at a given location, while the right-hand side represents fluxes due to diffusion. The velocities at each time-step are obtained from the Navier-Stokes equations, which is solved in tandem with Equation 21. The dye was added into the vessel at the same location as the dispersed fluid particles with an initial concentration of 1 mol/L. The dye is assigned a diffusion coefficient of 10^{-9} m^2/s, a value typical of binary liquids. (26)

The evolution of the dye concentration field is consistent with the evolution of the Lagrangian particles and the evolution of the reconstructed dispersed phase volume fraction. In principle, the consistency between these descriptions is expected, as both particle and scalar motion in the tank is dominated by the agitating effects of the impeller. In practice, this alignment reaffirms the ability to reconstruct the time-evolution of continuous fluid variables (*i.e.* volume fraction) using a suitably large number of discrete Lagrangian particles.

4.3 Calculating local fluid properties

We next examine a similar blending process, but now with density and viscosity differences between the two fluids. The impeller speed in this system is set to 100 RPM, intentionally lower than the 400 RPM cases considered above. The kinematic viscosity and density of the continuous phase are still taken to be 10^{-6} m^2/s and 1000 kg/m^3. The kinematic viscosity and density of the dispersed phase, however, are now taken to be 10^{-4} m^2/s and 900 kg/m^3. The initial dispersed phase volume was again described by 2,000,000 individual droplets with an

initial droplet diameter $D_{T,o}$ of 0.334 mm. Particle breakup and coalescence remain disabled in this simulation.

In Figure 8, we show the time-evolution of the dispersed phase volume fraction and the corresponding fluid density across the tank. At the start of the simulation, the step change in volume fraction at the interface between the fluids is apparent. With increasing time, the effects of buoyancy cause the dispersed phase to separate. That is, the pumping action of the impeller is insufficient to overcome the density difference between the (heavy) continuous phase and the (light) dispersed phase. Consequently, a stratified layer of dispersed fluid forms at the top of the vessel. As expected, for this non-reacting system with no mass-transfer, this stratification process does not change the total volume of the dispersed fluid. Moreover, throughout the separation process, the dispersed fluid volume fraction does not exceed 1.0. The cherry-pit particles are correctly preserving the incompressibility of the dispersed fluid while predicting proper volume fractions.

The stratification of these two fluids at this operating condition is in-line with *a priori* expectations. For two-fluid systems, the competition between fluid motion and fluid buoyancy can be characterized using the Richardson number, Ri: (25)

$$Ri = \frac{(\rho_H - \rho_L) g H}{\rho_H N^2 D^2} \qquad \text{Eqn. (22)}$$

where g is the acceleration due to gravity, H is the height of the tank, N is the impeller speed, and D is the impeller diameter. For $Ri \gg 1$, buoyancy effects are expected to dominate, such that the two fluids will tend to remain stratified (over timescales relative to the single fluid blend time). For $Ri \ll 1$, fluid inertia is expected to dominate, such that the two fluids will blend in a timescale that is commensurate with the single fluid blend time. The Richardson number for this system is 32, meaning the fluid is expected to remain stratified. Beyond corroborating the basic behavior of the E-L model, this result reaffirms an important point: to form droplets, the dispersed fluid must engage with the impeller. If, due to density effects, the impeller cannot draw fluid into the trailing vortex, discussions about the droplet size distribution are irrelevant.

Two topics are worth recognizing before extending the model to handle systems with droplet breakup and coalescence. First, because the volume fraction is reconstructed from a discrete particle field, the interface presents no spurious numerical diffusion. Thus, even for systems with very small quantities of dispersed fluid, there is no premature blending and/or mixing due to insufficient control over scalar transport along the interface. Thus, although presented here within the context of an immiscible system, this approach can be generally useful when predicting the mixing behavior of a small quantity of two fluids where diffusion can be ignored. Second, missing from this approach is the cohesive effect of surface tension on the initial dispersed fluid during early states of the simulation. As discussed below, the effects of surface tension can be directly incorporated into particle breakup and coalescence. The initial dispersed injection, however, is represented as a group of many individual droplets. The lack of tension between the droplets implies that the initial injection will breakup into its constituent droplets more quickly than a continuous fluid. Provided the initial bubbles are large relative to the equilibrium droplet size, however, the effects of this initial breakup are not expected to have a large influence on the time-evolution of the dispersion process.

4.3 Incorporating Breakup and Coalescence

The results presented above indicate that dispersed phase particles, as represented by the cherry-pit model, can be used to reconstruct the continuous dispersed phase volume fraction. From this phase field, dispersions involving fluids with differing densities and viscosities can be handled directly within the model. Beyond reproducing the volume fraction, however, the particles can undergo breakup and coalescence to predict the time-evolution of the droplet size distribution. Predictions from the direct two-fluid model provide a framework for incorporating discrete droplet breakup events into the E-L model.

We now describe the breakup kernel. Motivated by the semi-empirical relationship presented in Equation 3, which was corroborated by output from the direct two-fluid model presented in Figure 3, we define a critical droplet diameter, d_m, as:

$$d_m = 0.725 \frac{\sigma^{\frac{3}{5}}}{\rho^{\frac{3}{5}} \epsilon^{\frac{2}{5}}}.$$ Eqn. (23)

This diameter defines the upper bound on the droplet size allowed within a given region of the fluid. If a droplet enters a fluid cell wherein the local and instantaneous d_m defined by Equation 23 is smaller than the current droplet diameter, a breakup event is initiated. This breakup produces two new droplets. The volume fraction of the first daughter particle is randomly sampled from the distribution function generated by the Unified Breakup Model, which is calculated on-the-fly using the fluid properties, current droplet diameter, and the energy dissipation rate surrounding the droplet. To conserve volume, the volume fraction of the second daughter is set to the complement of the first.

The system modeled here is assumed to be actively coalescing. That is, if two droplets collide, they are always assumed to combine into a single droplet with a new volume equal to the total volume of the two colliding droplets. In principle, since particle interactions are tracked explicitly, more sophisticated rules governing pair-wise coalescence versus a pair-wise bounce may be specified. (35) Also, recognize that, within the E-L approach, it is straightforward to deactivate droplet coalescence altogether. This deactivation is evoked below when modeling electrolytic solutions, which are known to inhibit coalescence at modest (>0.1M) salt concentrations. (36)

With these breakup and coalescence models active, we re-ran the 1 L simulation presented in Figure 1 at an impeller speed of 400 RPM using the E-L model. The kinematic viscosity and density of both fluids were set to 10^{-6} m^2/s and 1000 kg/m^3. The surface tension between the fluids was set to 0.04 N/m. We superimpose on Figure 4 the steady-state droplet size distribution predicted from this E-L simulation after 10 seconds of agitation to that predicted from the direct two-fluid simulations. The shapes of both distribution functions are similar, with a most probable particle diameter inline with experimentally measured values for this operating condition. This result suggests that the breakup and coalescence models applied within the E-L model are sufficiently reproducing the breakup and coalescence physics realized in the direct two-fluid model. Because the model can support a much coarser lattice resolution,

however, the E-L model computes the steady state droplet size distribution two orders-of-magnitude faster than the direct two-fluid model.

4.5 Predicting Droplet Size Distributions

Beyond reproducing results from the direct two-fluid model, the speed improvements introduced by the E-L approach allow us to directly model the 2-gallon agitated system used by Sprow to develop the design correlation presented in Equation 4. (5) This system, as illustrated in Figure 1, is geometrically similar but approximately 8x larger by volume than the systems considered in Sections 3 and 4. The tank is agitated by a 0.076 m diameter flat blade impeller. Impeller speeds were set to 250, 300 and 500 RPM. The continuous phase was salt water with a density of 1005 kg/m^3 and a viscosity of 10^{-6} m^2/s. The dispersed phase was iso-octane with a density of 692 kg/m^3 and a viscosity of $7x10^{-7}$ m^2/s. The surface tension between the two fluids is 0.042 N/m. The volume fraction of the dispersed phase was set to 0.005. These parameters are consistent with the experiment.

The lattice spacing was again set to 150 points across the tank diameter. The Courant number was set to 0.1. These discretization parameters are sufficient to properly resolve the blend time, shaft power and energy dissipation in this system. Coalescence was deactivated in the simulation, which mimics the non-coalescing environment realized in the experimental configuration. Mechanistically, this response was modeled by only allowing particle diameters to decrease. The dispersed phase was reconstructed using 233,016 individual particles with an initial diameter set to 2.1 mm (corresponding to $D_{P,o} = \Delta x/2$).

In Figure 9, we compare the predicted variation in mean droplet diameter with impeller speed to the measured data at these same operating conditions. We superimpose on this prediction the experimentally derived correlation by Sprow, which was developed in part using this measured data. For each case, the simulated time required to achieve a steady-state droplet size distribution was on the order of 1-2 hours (20,000-40,000 impeller turns). This timescale, which is consistent with the experimental report, (5) is correlated to the time required for all

droplets to equilibrate with the energy dissipation extrema in the trailing vortex. The mean droplet diameter predicted from the model is 15-30% higher than the measured data for the three operating conditions considered here. Although the bias is noted, the difference is consistent with the measurement uncertainty. Moreover, consistent with the measured data and with expectations from the design correlation, the mean droplet diameter predicted from the simulation decreases as $N^{-\frac{6}{5}}$. In Figure 10, we compare the predicted to measured droplet diameter distribution for the 500 RPM operating condition during steady state operating conditions. The data are presented as histograms describing the cumulative volume fraction of the dispersed phase. Conceptually speaking, for a specific diameter d^* on the x-axis, the corresponding value on the y-axis is the fraction of the dispersed phase fluid volume contained in droplets with diameters smaller than d^*. Both the predicted and measured distributions are non-symmetric. This behavior is expected for the non-coalescing system here. More specifically, the maximum energy dissipation rate within the trailing vortex establishes a maximum allowable droplet diameter. Below this maximum allowable diameter, however, variance is introduced by the non-uniform daughter volume fractions generated during breakup events.

Although the shape of the predicted distribution is consistent with the measured data, the model predicts less variance in droplet diameter than was measured experimentally. Although some of this difference may be related to topological differences between the modeled/experimental geometry, we suspect that most is related to the droplet breakup kernel. As discussed in Section 2 and presented in Figure 3, the Unified Breakup Model presents less variance in the daughter droplet diameters than predictions from the direct two-fluid model. This under-prediction of daughter droplets with volume fraction extrema has the net effect of decreasing the variance in the droplet population. We recognize that more sophisticated/tunable breakup kernels may be developed. The overall agreement between the predicted/measured values, however, suggests the Unified Breakup Model is predicting satisfactory daughter droplet volume fractions.

4.6 Advantages and Disadvantages

The E-L model approach reproduces many droplet properties expected from the direct two-fluid model. The approach can be used to reconstruct a continuous dispersed phase volume fraction as well as the corresponding variations in liquid density and viscosity. With breakup/coalescence active, the approach can reproduce the findings predicted from the direct two-fluid model, in terms of the most-probable droplet diameter and droplet size distribution. The predicted relationship between impeller speed and droplet diameter is also consistent with measured data. Since breakup and coalescence are described via user-defined kernels, it is straightforward to isolate the effects of these competing physics on the realized droplet distribution. This decomposition is more difficult within the context of a two-fluid model.

Unlike the direct two-fluid model, which is limited by lattice spacing, the E-L approach is limited by particle count and particle tracking/breakup/coalescence compute time. On a compute node with 4 NVIDIA V100 GPUs, the two-fluid simulation advanced at approximately 200 million particle updates per second. This speed corresponds to about 100 impeller turns per day of compute time for the 1 L system operating at 400 RPM. In principle, the total simulation capacity on this compute node is approximately 200 million individual droplets. In practice, however, only 100 mL of fluid dispersed uniformly into 0.1 mm droplets corresponds to about 191 million particles. Dispersion of larger fluid volumes into smaller droplets would increase the particle population beyond computational practicality. These effects limited our ability to reproduce the data measured by Sprow at higher impeller speeds. Thus, although the E-L model presents speed and volume improvement over the direct two-fluid model, further generalizations are required to extend the approach to handle larger dispersed phase particle populations.

5.0 Parcel/Eulerian Simulations

5.1 Conceptual Overview

To extend the E-L model to support systems with a larger number of individual droplets, we can further generalize the approach to support droplet *parcels*. A droplet parcel is a single Lagrangian point object that represents the motion of a group of individual droplets. This approach has been used previously to investigate granular flows, hydrodynamics in gas-solid flows, and fluidized beds. (37) Like individual droplets, a parcel is defined by a parcel density and parcel diameter---properties that define its trajectory and dynamics. In addition to these kinematic properties, however, each parcel is further characterized by a parcel number scale. This number scale, which quantifies the number of equal-sized droplets contained within the parcel, adjusts dynamically during breakup/coalescence events to conserve total droplet volume. The dispersed phase in the parcel approach is still modeled using many individually tracked Lagrangian objects which undergo breakup and coalescence events. The net effect of the coarse graining, however, is a reduction in the number of explicitly tracked particles and reduced computational burdens.

5.2 Mathematical Description

Mechanistically, fluid transport in the E-P model is identical to fluid transport in the E-L model. The generalization from droplet particle to droplet parcel, however, requires three key adjustments. First, since a parcel contains multiple real droplets, the local fluid volume fraction defined must be generalized to become:

$$\phi_{d,j} = \frac{\sum_i^{i \in j} L_i V_{P,i}}{V_j}. \qquad \text{Eqn. (24)}$$

where L_i is the number scale of parcel i. The second adjustment is to the force on the fluid from the parcel. As a modification to Equation 20, the force on the fluid from the parcel is now a function of the parcel number scale:

$$\vec{F}_{f,j} = -\sum_i^{i \in j} L_i \left(\vec{F}_{i,a} + \vec{F}_{i,D}\right), \qquad \text{Eqn. (25)}$$

where $i \in j$ is the set of parcels with centers of mass contained in voxel j.

The third adjustment is to breakup and coalescence. Droplet breakup, if active, follows the approach presented for the E-L model: if a parcel enters a region wherein the local and instantaneous d_m defined by Equation 23 is smaller than the current parcel diameter, a

breakup event is initiated. The new parcel diameter is then randomly sampled from the distribution function generated by the Unified Breakup Model, which is calculated on-the-fly using the fluid properties, the original parcel diameter, and the surrounding energy dissipation rate. Within the E-P model, however, a new/explicitly tracked droplet is not generated. Instead, to conserve parcel volume, the number scale following a breakup event is modified to:

$$L_i(t) = L_{i,o}\left(\frac{d_{i,o}}{d_i(t)}\right)^3 \qquad \text{Eqn. (26)}$$

where $d_i(t)$ is the instantaneous parcel diameter (post-breakup), $d_{i,o}$ is the initial parcel diameter, and $L_{i,o}$ is the initial parcel number scale. Equation 26 ensures that the total droplet volume within each parcel is conserved over time.

Droplet coalescence can likewise be active or inactive in the E-P model. Since not all particles are tracked explicitly, however, the coalescence kernel must be a function of the local fluid properties and/or time-history of the fluid properties sampled by the parcel. The net effect of the kernel will be to increase the particle diameter while decreasing the parcel number scale. In the limit of actively coalescing systems with droplet mean free paths that are small compared to the droplet diameter, instantaneous and local droplet diameters will be equal to the local d_m defined by Equation 23. For electrolytic solutions or systems with low dispersed phase volume fractions, the effects of coalescence can be ignored. Between these two extremes, a user-defined coalescence relationship must be developed using predictions from a two-fluid model and/or measured data.

5.3 Model Set-up

We continue with the direct comparison to the measured data by Sprow. (5) The computational efficiencies introduced by the E-P approach, however, allow us to model the system at higher impeller speeds (which increases the droplet count to populations that exceed what is practical using the E-L approach). This system is the same 2 gallon system presented in Figure 1 with the same fluid properties. The impeller speeds considered here range from 250 to 2000 RPM---the full spectrum considered in the experiment.

As with the E-L simulations, the lattice spacing was set to 150 points across the tank diameter, which corresponded to a grid spacing of 4.2 mm. The Courant number was set to 0.1. Coalescence was deactivated in the simulation, which mimics the non-coalescing chemistry realized in the experimental configuration. Mechanistically, this behavior was modeled by only allowing parcel diameters to decrease, as permitted by Equation 23. We set ε to the instantaneous value surrounding each parcel, implying instantaneous droplet breakup due to increases in the surrounding local energy dissipation as parcels moved through the vessel. The dispersed phase was defined as 233,016 individual parcels, with an initial diameter set to 2.1 mm. The initial number scale set to 1.0, which corresponds to a total dispersed phase fluid volume of 3.6×10^{-6} m^3.

5.4 Model Output

We superimpose on Figure 9 the steady-state mean droplet diameter as a function of impeller speed, as predicted using the E-P model. Since the droplets are represented as parcels, the mean droplet diameter across the system is calculated from:

$$\bar{d} = \frac{\sum_i^{N_p} L_i d_i}{\sum_i^{N_p} L_i} \qquad \text{Eqn. (27)}$$

where N_p is the number of parcels in the system. Each system required approximately 30,000 impeller turns to reach a steady state droplet distribution, a duration consistent with the E-L models. We superimpose on this data the mean droplet diameter measured by Sprow at each operating condition, as well as the droplet diameter predicted from the experimentally derived design correlation. At each impeller speed, the predicted mean droplet diameter is within 25% of the measured value. Consistent with the measured data, the mean droplet diameter predicted from the E-P model decreases as $N^{-\frac{6}{5}}$.

In contrast to the mean droplet diameters predicted from the E-L model, which were elevated relative to expectations from the experimental correlation, the E-P model tends to predict smaller mean droplet diameters. This shift is related to differences in the droplet breakup process between the two models. Within the E-L approach, a mother droplet will undergo

pairwise breakup events until its diameter crosses below the threshold defined in Equation 23. Since the volume fraction of the daughter droplet is small relative to the mother droplet, the outcome of this process is one (or more) small droplet(s) along with a larger residual droplet with a diameter just below the threshold defined by Equation 23. In the E-P approach, *all* droplets represented by the parcel are scaled to the diameter of the smaller daughter; there is no large residual droplet with a diameter just below the threshold defined by Equation 23. The net effect of this difference is a smaller mean droplet diameter at the end of the breakup process. The experimental data, which sits between the predictions from the two methods, suggests that the behavior in the physical system may follow a hybridization of these two approaches.

In Figure 10, we present the steady state droplet size distributions predicted from the E-P model for impeller speeds of 500, 1000 and 2000 RPM. Like the E-L model, the shape of the predicted distribution and the corresponding shift with impeller speed are consistent with the measured data. The predicted distribution, again, presents less variance in droplet diameter relative to the experiment. As with the E-L model, we suspect this difference is related to an under sampling of the daughter droplet extrema in the Unified Breakup Model. The overall agreement between the predicted and measured mean droplet diameter and droplet size distributions, however, reinforce the generality of the modeling approach and associated breakup model.

5.5 Advantages and Disadvantages

Predictions from the E-P model are consistent with predictions from the E-L model. The output are likewise consistent with the measured variations in the mean droplet diameter with impeller speed and measured variations in the droplet diameter distribution. Like the E-L model, the E-P model requires a user-defined breakup kernel. This kernel can be motivated by predictions from two-fluid simulations and/or predictions from the Unified Breakup Model. Coalescence is less straightforward in the E-P model, since not all droplets are tracked individually. For non-coalescing systems, it is straightforward to deactivate coalescence

altogether. For actively coalescing systems or systems with high dispersed phase volume fractions, the instantaneous and local droplet diameters can be assumed to be equal to the local d_m defined by Equation 23. Between these extremes, more sophisticated coalescence kernels would need to be developed.

Because the number of tracked objects is limited to a constant number of parcels, the solver can advance quickly compared to the E-L model. On two NVIDIA V100 GPUs, each E-P simulation was able to predict a steady-state droplet size distribution after only a few hours of runtime. This limit on particle count also makes the E-P approach extensible to larger-scale vessels. In principle, the number of tracked parcels need only be sufficient to (i) reconstruct a continuous dispersed phase fluid volume fraction, and (ii) properly sample the energy dissipation landscape/droplet size distribution across the vessel. In most cases, these conditions can be mutually satisfied by setting the initial parcel diameter to the simulation lattice spacing. The total number of tracked parcels will therefore not exceed the total number of simulation lattice points. Under these conditions, the runtimes of the E-P simulations are expected to be order-of-magnitude consistent with the runtimes of a single-phase fluid simulation, which are routinely executed at working volumes that exceed 1000 L. (24)

6.0 Qualitative guidance and next steps

The self-consistency of the three approaches presented here is noteworthy, in terms of corroborating expectations from first-principles turbulence theory and reproducing key output from experimental data. Because each model takes a mechanistic approach to droplet transport and breakup, a change to the simulation operating conditions and/or scale does not require adjustment to the model set-up. Although hardware limitations may inform which modeling approach is selected, the predicted droplet size distribution and its variation with batch operating conditions are not expected to depend strongly on which modeling approach is applied. We also note that, given the generality of the Unified Breakup Model, the approach presented here is also extendable to gas-liquid simulations. This generalization is useful for predicting bubbles sizes in gasified bioreactors, and the associated mass transfer rates.

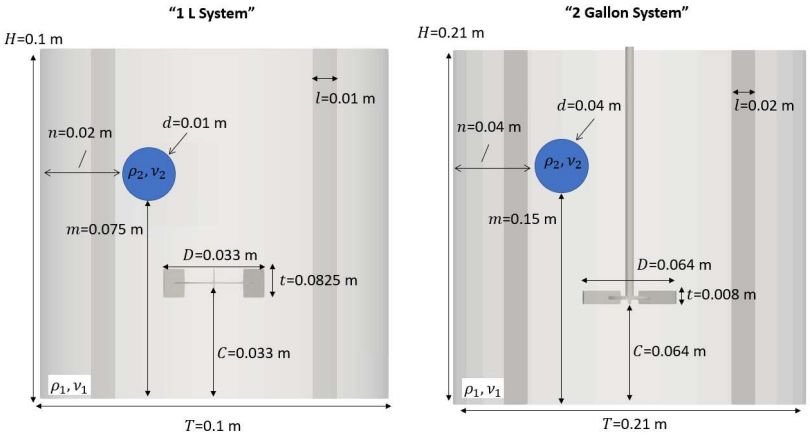

Figure 1: Two agitated tank systems considered in this work. Both systems are geometrically similar with approximate fluid volumes of 1 liter and 2 gallons, respectively. The smaller volume vessel is agitated by a Rushton impeller while the larger vessel is agitated by a flat blade turbine. At the start of the simulation, the volume fraction of the dispersed fluid (i.e., the value of ϕ) is set to 1.0 in the region inside the marked sphere. Outside this region, the volume fraction of the dispersed fluid is set to zero.

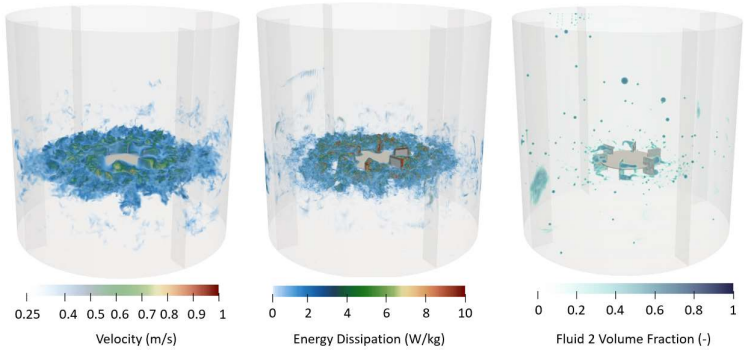

Figure 2. Output from the direct two-fluid simulation. Left: Instantaneous snapshot of fluid speed. Center: Snapshot of energy dissipation rate. Right: Snapshot of droplets. Images generated after 10 seconds of agitation.

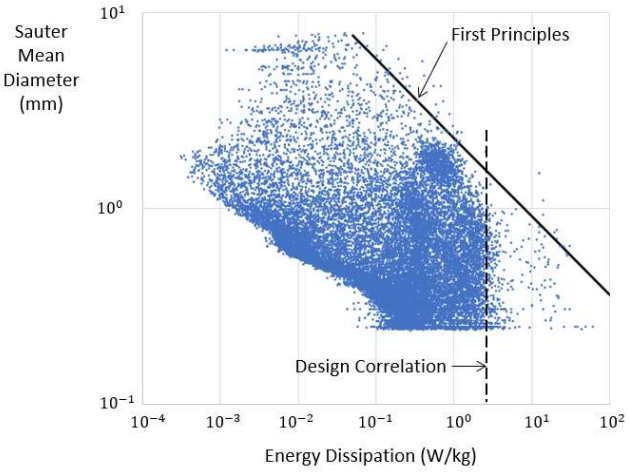

Figure 3: Scatter plot of Sauter mean droplet diameter versus surrounding energy dissipation rates. The variation in maximum droplet diameter with energy dissipation rate is consistent with expectations from the semi-empirical model presented as

Equation 3. (15) The energy dissipation rate sampled in the trailing vortex is consistent with experimentally derived design correlations, presented as Equation 15. (16)

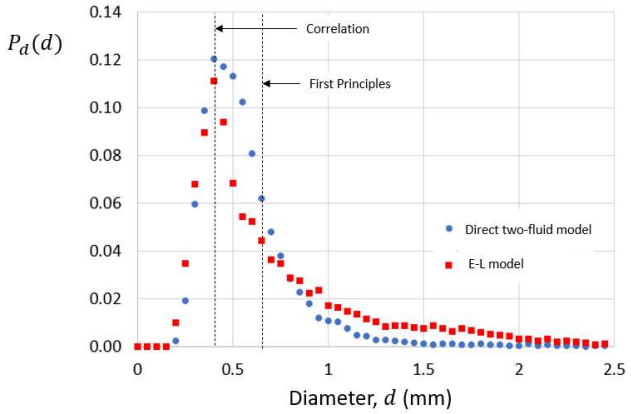

Figure 4: Probability density function of droplet diameters for the direct two-fluid simulation and the Eulerian-Lagrangian (E-L) simulations for the 1 L system agitated by a Rushton impeller. Superimposed on this data is the mean droplet diameter expected from first principles, as well as expectations from the Sprow correlation. (4)

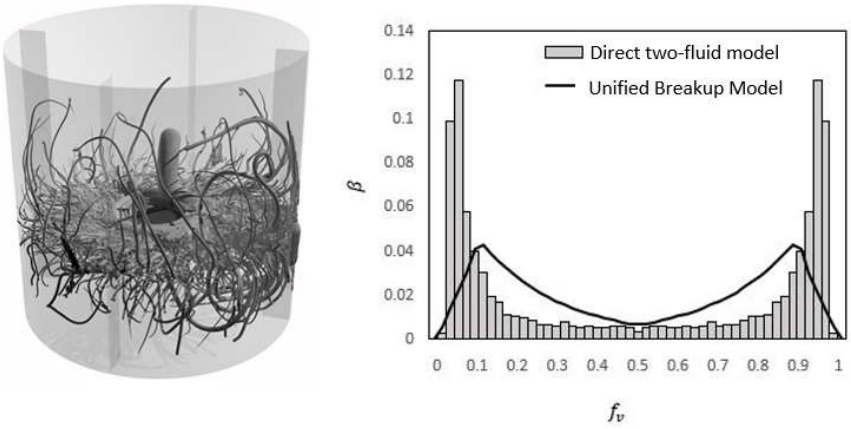

Figure 5: Left: Trajectory of droplets undergoing break-up within the trailing vortex. Right: Predicted histogram of daughter droplet volume fractions, f_v, following a binary breakup event. Superimposed on this predicted histogram is the daughter volume fraction probability distribution function calculated using the Unified Breakup Model. (29)

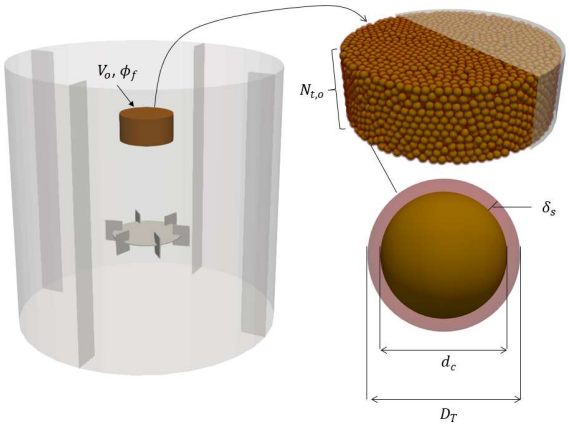

Figure 6: Illustration of the cherry-pit particles used in the E-L model and the reconstruction of the dispersed phase fluid volume.

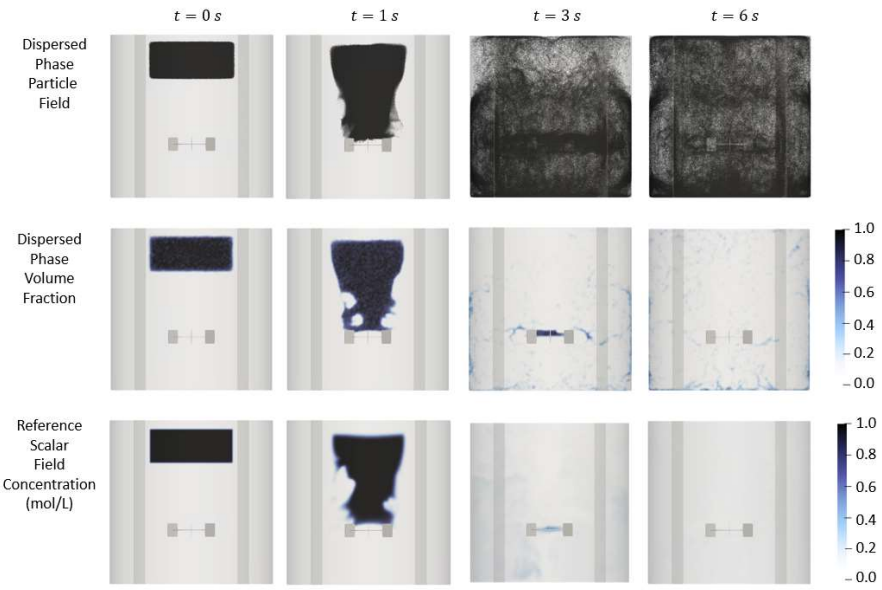

Figure 7: Two-fluid blending simulation. Top: Time-evolution of dispersed phase particles used to track the position of the second fluid. Center: Dispersed phase volume fraction, as reconstructed from the particle volume fraction. Bottom: Reference scalar field, advanced using the advection-diffusion equation.

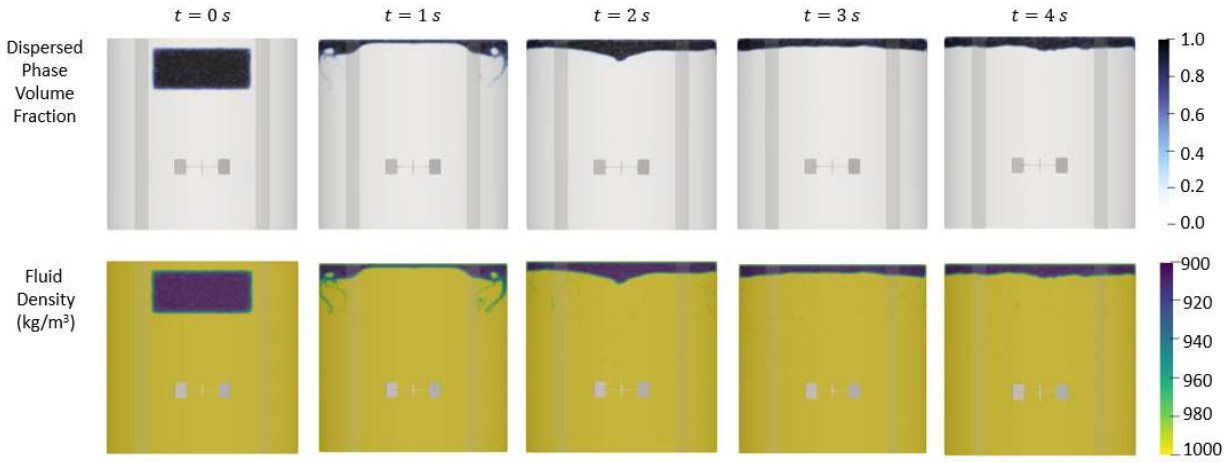

Figure 8: Density-driven stratification process. As expected from the Richardson number, the impeller speed is insufficient to overcome the buoyancy force separating the two fluids. The E-L model is correctly representing the effects of this density difference, while preserving incompressibility within the dispersed phase.

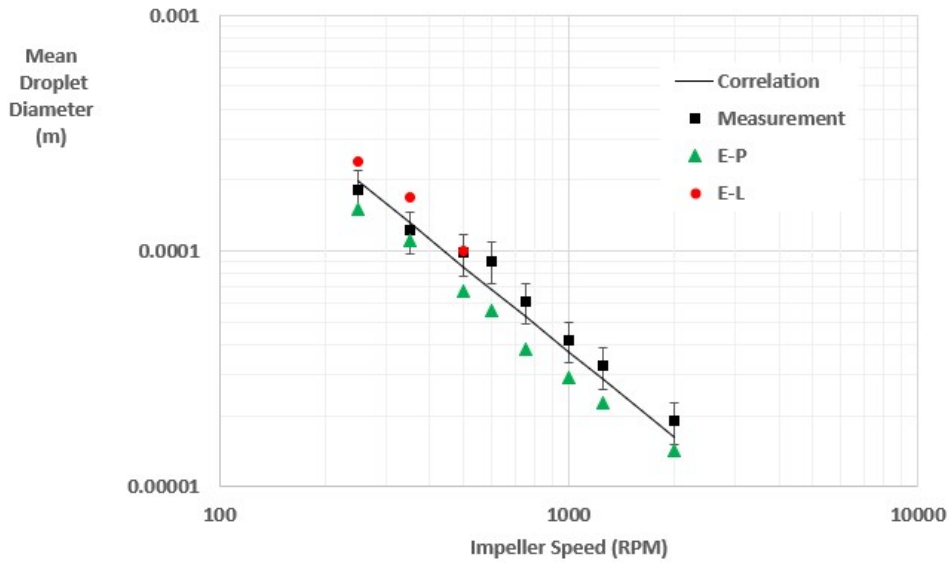

Figure 9: Variation in mean droplet diameter with impeller speed. Comparisons between design correlation, experimental measurement, predictions from the Eulerian-Lagrangian (E-L) method, and the Eulerian-Parcel (E-P) method.

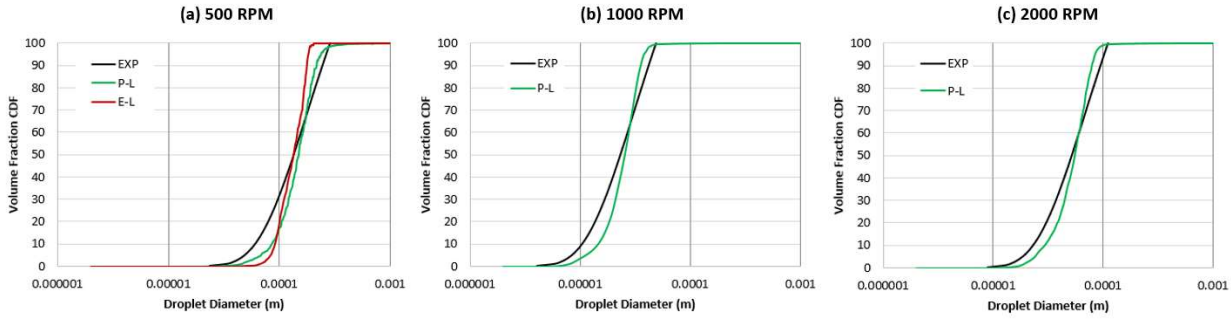

Figure 10: Variation in droplet size distribution at multiple impeller speeds. Comparisons between experimental measurement (EXP), predictions from the Eulerian-Lagrangian (E-L) simulations, and the Eulerian-Parcel (E-P) simulations.

List of Symbols

Greek

δ_x Lattice-spacing
δ_t Timestep
ε Specific energy dissipation rate
μ Dynamic viscosity
$\nu_{e,i}$ Eddy viscosity
ρ Density
ρ_H Heavy fluid density
ρ_L Light fluid density
σ Surface Tension
τ Torque
τ_f Relaxation time
ϕ Volume fraction
ϕ_j Dispersed phase volume fraction
ϕ_p Hard sphere packing fraction
ω Angular velocity

Latin

$\vec{a}_i$ Acceleration of particle
D_T Diameter of the dispersed phase droplets
C_m Courant number
C_s Smagorinsky coefficient
c Species concentration
D Impeller diameter or Species Diffusion coefficient
D_m Maximum Diameter
d_c Particle core diameter
d_m Mean diameter
d_{32} Sauter mean diameter
E_t Total energy dissipation rate
$\vec{F}_b$ Body force
$\vec{F}_{i,a}$ Added mass force on particle
$\vec{F}_{i,D}$ Drag force
$\vec{F}_{i,g}$ Gravity force on particle
$\vec{F}_{ij}$ Interparticle contact force
$\vec{F}_{i,p}$ Pressure gradient force
$\vec{F}_s$ Surface force
f Component of the probability density function
f^0 Equilibrium probability density function
f_v Droplet daughter volume fraction
g Gravity
H Fluid height
k_{ij} Stiffness co-factor
L_i Number scale
M mobility parameter
m_i Mass of particle
N Impeller RPM
N_t Total number of particles
$\vec{n}$ Surface normal
P_o Impeller power number
p Fluid pressure
$\bar{S}$ Norm of the strain rate tensor
u Speed
V_o initial volume of dispersed phase fluid
V_r Reference velocity
v Velocity
W Interface width
w_p Width of impeller blade
$\vec{x}$ Position
Y Elastic modulus

Acronyms

CPU Central Processing Unit
GPU Graphics Processing Unit
E-L Eulerian Lagrangian Model
E-P Eulerian Parcel Model
PBM Population balance models
RANS Reynolds Average Navier-Stokes
We Weber Number
Ri Richardsen Number

Works Cited

1. **Doran, Pauline M.** *Bioprocess Engineering Principles 2nd Edition.* s.l. : Academic Press, 2012.

2. *Drop breakup by impellers.* **Wichterle, Kamil.** 1995, Chemical Engineering Science, pp. 3581-3586.

3. *PHASE INVERSION AND ASSOCIATED PHENOMENA.* **Leslie Y. Yeo, Omar K. Matar, E. Susanna Perez de Ortiz, Geoffrey F. Hewitt.** 1, s.l. : Multiphase Science and Technology, 2000, Vol. 12.

4. *Drop size distributions in strongly coalescing agitated liquid-liquid systems.* **Sprow, F. B.** 1967, AiChE Journal, pp. 995-998.

5. *Distribution of drop sizes produced in turbulent liquid—liquid dispersion.* **Sprow, F.B.** 1967, Chemical Engineering Science, pp. 435-442.

6. *Droplet size distribution and mixing hydrodynamics in a liquid–liquid stirred tank by CFD modeling.* **Pakzad, Sepehr Khajeh Naeeni and Leila.** 2019, International Journal of Multiphase Flow, p. 103100.

7. *Local gas holdup simulation and validation of industrial-scale aerated bioreactors.* **Witz, Christian, Daniel Treffer, Timo Hardiman, and Johannes Khinast.** 2016, Chemical Engineering Science, pp. 636-648.

8. *GPU-accelerated large eddy simulation of stirred tanks.* **Yang, Shuli Shu and Ning.** 2018, Chemical Engineering Science, pp. 132-145.

9. *GPU-accelerated transient lattice Boltzmann simulation of bubble column reactors.* **Shu, Shuli, Jingchang Zhang, and Ning Yang.** 2020, Chemical Engineering Science, p. 115436.

10. *Review on gas-liquid mixing analysis in multiscale stirred vessel using CFD.* **Shah, Raja Shazrin Shah Raja Ehsan.** 2012, Reviews in Chemical Engineering, pp. 171–189.

11. *Investigations on hydrodynamics and mass transfer in gas–liquid stirred reactor using computational fluid dynamics.* **Sivaraman, Panneerselvam Ranganathan and Savithri.** 2011, Chemical Engineering Science, pp. 3108-3124.

12. *Efficient neighbor list calculation for molecular simulation of colloidal systems using graphics processing units.* **Michael P.Howard, Joshua A. Anderson, Arash Nikoubashman, Sharon C.Glotzer, Athanassios Z.Panagiotopoulos.** 2016, Computer Physics Communications, pp. 45-52.

13. *Mathematical models for design of bioreactors: Applications of: Kolmogoroff's theory of isotropic turbulence.* **Moo-Young, Y. Kawase and M.** 43, 1990, The Chemical Engineering Journal, Vol. 1, pp. 19-41. .

14. **Pope, Stephen B.** *Turbulent Flows.* s.l. : Cambridge University Press, 2000.

15. *Fundamentals of the hydrodynamic mechanism of splitting in dispersion processes.* **Hinze, J. O.** 3, 1955, AIChE Journal, Vol. 1, pp. 289-295.

16. *Mixing: Impeller performance in stirred tanks.* **Grenville, R., Giacomelli, J., Padron, G., Brown, D.A.R.** 2017, Chem. Eng. , pp. 42–51.

17. *A conservative phase field method for solving incompressible two-phase flows.* **Lin, Pao-Hsiung Chiu and Yan-Ting.** 1, 2011, Journal of Computational Physics, Vol. 230, pp. 185-204.

18. **Krüger, T., Kusumaatmaja, H., Kuzmin, A., Shardt, O., Silva, G., Viggen, E.M.** *The Lattice Boltzmann Method.* s.l. : Springer International Publishing, 2017.

19. **Succi, Sauro.** *The lattice Boltzmann equation: for fluid dynamics and beyond.* s.l. : Oxford University Press, 2001.

20. **Shu, Zhaoli Guo and Chang.** *Lattice Boltzmann method and its applications in engineering.* s.l. : World Scientific, 2013.

21. *An immersed boundary method based on the lattice Boltzmann approach in three dimensions, with application.* **Zhu, Luoding, Guowei He, Shizhao Wang, Laura Miller, Xing Zhang, Qian You, and Shiaofen Fang.** 12, 2011, Computers & Mathematics with Applications, Vol. 61, pp. 3506-3518.

22. *DNS and LES of decaying isotropic turbulence with and without frame rotation using lattice Boltzmann method.* **Huidan Yu, Sharath S. Girimaji, and Li-Shi Luo.** 2, 2005, Journal of Computational Physics , Vol. 209, pp. 599-616.

23. *M-Star CFD User Manual.* **M-Star Simulations.** 2020.

24. *A mechanistic approach for predicting mass transfer in bioreactors.* **John A. Thomas, Xiaoming Liu, Brian DeVincentis, Helen Hua, Grace Yao, Michael C. Borys, Kathryn Aron, Girish Pendse.** 2021, Chemical Engineering Science, p. 116538.

25. *A CFD Digital Twin to Understand Miscible Fluid Blending.* **John Thomas, Kushal Sinha, Gayathri Shivkumar, Lei Cao, Marina Funck, Sherwin Shang and Nandkishor Nere.** 2021, AAPS PharmSciTech, p. 91.

26. **Lide, David R.** *CRC handbook of chemistry and physics.* s.l. : CRC press, 2004. Vol. 85.

27. **Ma, Zheng.** *Impeller power draw across the full Reynolds number spectrum.* M.S. Thesis : University of Dayton, 2014.

28. *Experiments on breakup of bubbles in a turbulent flow.* **Jiří Vejražka, Mária Zedníková, and Petr Stanovský.** 2018, AiChE Journal, pp. 740–757.

29. *A unified theoretical model for breakup of bubbles and droplets in turbulent flows .* **Chutian Xing, Tiefeng Wang, Kunyu Guo, and Jinfu Wang.** 4, 2015, AIChE Journal, Vol. 61, pp. 1391-1403. .

30. *SIMPLE FORMULAS FOR POROSITY AND SPECIFIC SURFACE OF THE CHERRY-PIT MODEL.* **D. Stoyan, H. Hermann, Antje Elsner.** 2019, Journal of Porous Media, pp. 387-394.

31. *Physics of Granular States.* **Nagel, H. M Jaeger and S. R.** 1992, Science, p. 1524.

32. *A coupled lattice Boltzmann method and discrete element method for discrete particle simulations of particulate flows.* **Rüde., Christoph Rettinger and Ulrich.** 2018, Computers & Fluids , Vol. 172, pp. 706-719.

33. **Tildesley., Michael P Allen and Dominic J.** *Computer simulation of liquids.* 2nd. s.l. : Oxford University Press, 2017.

34. **Strand, Aaron.** *Investigation of Blend Time for Turbulent Newtonian Fluids in Stirred Tanks.* Mechanical Engineering . s.l. : Rochester Institute of Technology, 2017. MS Thesis.

35. *Laws of bubble coalescence and their modeling.* **Boshenyatov, Boris.** 4, 2013, Journal of Magnetohydrodynamics and Plasma Research, Vol. 18, p. 311.

36. *Effect of Electrolytes on Bubble Coalescence in Columns Observed with Visualization Techniques.* **RAMOS, MARÍIA EUGENIA AGUILERA ANTONIETA OJEDA CAROLINA RONDÓN AURA LÓPEZ DE.** 2002, Annals of the New York Academy of Sciences, pp. 242–246.

37. **Clayton T. Crowe, John D. Schwarzkopf, Martin Sommerfeld, Yutaka Tsuji.** *Multiphase Flows with Droplets and Particles.* s.l. : CRC Press, 2012.

38. *Single drop breakup in turbulent flow.* **Komrakova, Alexandra E.** 2019, The Canadian Journal of Chemical Engineering, pp. 2727-2739.

39. *Euler–Lagrange modeling of a gas–liquid stirred reactor with consideration of bubble breakage and coalescence.* **R. Sungkorn, J. J. Derksen, and J. G. Khinast.** 5, 2012, AIChE Journal, Vol. 58, pp. 1356-1370.

40. **Mohamad, A. A.** *Lattice Boltzmann Method.* London : Springer, 2011.

41. *Composition-dependent thermodynamics of intracellular phase separation.* **Riback, J.A., Zhu, L., Ferrolino, M.C. et al.** 2020, Nature , pp. 209–214.

42. *A description ofphase inversion behaviour in agitated liquid–liquid dispersions under the influence ofthe Marangoni effect.* **Leslie Y. Yeo, Omar K. Matar, E. Susana Perez de Ortiz, Geoffrey F. Hewitt.** 2002, Chemical Engineering Science, pp. 3505 – 3520.

43. *Lattice Boltzmann simulations for multi-scale chemical engineering.* **HE., Van den Akker.** 67-75, s.l. : Current Opinion in Chemical Engineering, 2018, Vol. 21.